CrossMark

Impact of Interdecadal Pacific Oscillation on Indian summer monsoon rainfall: an assessment from CMIP5 climate models

Manish K. Joshi[1] · Fred Kucharski[2,3]

Abstract The present study evaluates the fidelity of 32 models from the fifth Coupled Model Intercomparison Project (CMIP5) in simulating the observed teleconnection of Interdecadal Pacific Oscillation (IPO) with Indian summer monsoon rainfall (ISMR). Approximately two-thirds of the models show well-defined spatial pattern of IPO over the Pacific basin and most amongst these capture the IPO-ISMR teleconnection. In general, the models that fail to reproduce the IPO-ISMR teleconnection are the ones that are also showing a poor spatial pattern of IPO, irrespective of the extent to which they reproduce the precipitation climatology and seasonal cycle. The results reveal a strong relationship between the quality of reproducing the IPO pattern and the IPO-ISMR teleconnection in the models, in particular with respect to the tropical–extratropical as well as the equatorial Pacific-Indian Ocean sea surface temperature gradients during IPO phases. Furthermore, the CMIP5 models that are capable of reproducing the IPO-ISMR teleconnection also reasonably simulate the atmospheric circulation as well as the convergence/divergence patterns associated with the IPO. Thus, for the better understanding of decadal-to-multidecadal variability and to improve decadal prediction of rainfall over India it is therefore vital that models should simulate the IPO skillfully.

✉ Manish K. Joshi
manishkumarjoshi@gmail.com; manishkjoshi@tropmet.res.in; dr.manishkjoshi@gmail.com

[1] Centre for Climate Change Research, Indian Institute of Tropical Meteorology, Pune, Maharashtra 411008, India

[2] Earth System Physics Section, Abdus Salam International Center for Theoretical Physics, Trieste, Italy

[3] Center of Excellence for Climate Change Research, Department of Meteorology, King Abdulaziz University, Jeddah, Saudi Arabia

1 Introduction

Natural climate variability at decadal-to-multidecadal timescales in the Pacific Ocean is termed as the Pacific decadal variability, which is generally referred as the Interdecadal Pacific Oscillation (IPO; Power et al. 1998, 1999; Allan 2000; Folland et al. 1999) for the basin-wide pattern, or the Pacific Decadal Oscillation (PDO; Mantua et al. 1997) for the North Pacific pattern. The time series of IPO is analogous to the PDO index of Mantua et al. (1997). The signature of warm (cold) phase of IPO is characterized as warm (cold) SST anomalies (SSTAs) in the tropical Pacific and cold (warm) SSTAs in the central North Pacific (Trenberth and Hurrell 1994; Meehl et al. 2009).

The regional climate is significantly influenced by the large-scale climate variability in the Pacific region. Many preceding studies (e.g., Power et al. 1999; Folland and Salinger 1995; Salinger and Mullan 1999; Dai 2013) have shown that the IPO acts as a modulator of climate in many parts over the globe. The IPO has immense impact on precipitation as well as on other climate variables. It strongly modulates the teleconnection between El Niño-Southern Oscillation (ENSO) and precipitation on yearly basis over Australia (Power et al. 1999) and the sub-bidecadal climate variations, which were also recognized in the temperature signal (Folland and Salinger 1995), over New Zealand (Salinger and Mullan 1999). The IPO-like variability also modulates the ENSO teleconnections on interdecadal timescales over North America (Gershunov and Barnett 1998).

$\underline{\textcircled{2}}$ Springer

Over West and Central United States (especially the South-west), decadal precipitation variations also follow the IPO, i.e., the warm (cold) phase of IPO is linked with wet (dry) periods of rainfall (Dai 2013).

There is a large variability in the Indian summer monsoon rainfall (ISMR) and this variability is related with SSTAs over different oceanic basins at multiple timescales (Rasmusson and Carpenter 1983; Shukla 1987; Shukla and Paolino 1983; Krishnamurthy and Goswami 2000; Joshi and Rai 2015). At interdecadal timescales, ISMR shows alternate epochs of above- and below-normal rainfall each lasting for about three decades or so (Kripalani et al. 1997; Krishnamurthy and Goswami 2000; Goswami 2005). The interdecadal variation of ISMR is strongly correlated with interdecadal variations of ENSO (Krishnamurthy and Goswami 2000). Krishnan and Sugi (2003) found an inverse relationship between the interdecadal fluctuations of Pacific Ocean SST and Indian monsoon rainfall. Kucharski et al. (2009) stated that the tropical Pacific related SSTs force the decadal monsoonal variability over Indian region. Based on long observational records, Joshi and Pandey (2011) reported that the cold phase of IPO is associated with increase in rainfall over Indian region. Joshi and Rai (2015) found that the negative phase of IPO enhances the rainfall over west central, northwest, and peninsular regions of India, while over northeast region it causes reduction of rainfall. Further, it was stated that during the cold phase of IPO the southwesterlies over Indian region get strengthened by the easterlies from the equatorial Pacific.

However, up to now, only few studies have analyzed the simulated impact of IPO on Indian monsoon rainfall in Coupled General Circulation Models (CGCMs). In a 1360-year control run of a global coupled climate model, Meehl and Hu (2006) found large multidecadal variations in precipitation over India and reported that these variations are linked to multidecadal SST variations in the Pacific that resemble the observed IPO. Using observations and coupled model simulation, Krishnamurthy and Krishnamurthy (2014) investigated the relation between Indian summer monsoon and the IPO-like variability observed in SST of the North Pacific Ocean and reported that its warm (cold) phase is associated with deficit (excess) rainfall over India.

Multi-model products from the fifth Coupled Model Intercomparison Project (CMIP5; Taylor et al. 2012) provide state-of-the-art model simulations to scrutinize teleconnections over multiple timescales. The capability of climate models in simulating the key modes of natural variability and their teleconnection provides essential ground for the interpretation and use of climate change projection. Recently, many studies have been performed to assess the fidelity of models in evaluating teleconnections between the Pacific basin SSTs and the climate of Sahel and North America (Sheffield et al. 2013; Polade et al. 2013;

Villamayor and Mohino 2015; Fuentes-Franco et al. 2015). The observation as well as CMIP5 simulations show that the warm phase of IPO leads to a drought like condition over Sahel (Mohino et al. 2011; Villamayor and Mohino 2015). Sheffield et al. (2013) evaluated CMIP5 historical simulations of intraseasonal to multidecadal variability and teleconnections with North American climate and reported that the models capture the spatial pattern of IPO-like variability and its influence on continental temperature and West Coast precipitation. Dong et al. (2014) analyzed CMIP5 model realizations to explore the relative contributions of internal variability, greenhouse gases (GHGs), and anthropogenic aerosols (AAs) in driving the magnitude and evolution of interdecadal variability in the Pacific during the twentieth century and reported that its phase transition is dominated by internal variability and also significantly affected by external forcing agents such as GHGs and aerosols. Dong and Dai (2015) examined the influence of IPO on temperature and precipitation using observational and reanalysis data as well as model simulations and reported that more than half of the interdecadal variations in temperature and precipitation over northeastern Australia, western Canada, and northern India are explained by the IPO.

In the present study, the impact of IPO on Indian rainfall has been scrutinized using the historical simulations of 32 models that participated in the CMIP5 (Taylor et al. 2012). This study addresses the following issues: (1) Are the CMIP5 models under consideration capable of simulating IPO? (2) Do the CMIP5 models have capability to reproduce the IPO-ISMR teleconnection? (3) Is there any relationship between the quality of reproducing IPO and IPO-ISMR teleconnection in the models? (4) Are the CMIP5 models capable of reproducing the atmospheric circulation and the convergence/divergence patterns associated with the IPO?

The datasets used in the present study are discussed in Sect. 2. The method of analysis is elucidated in Sect. 3. Results evaluating the models fidelity in representing the IPO-ISMR teleconnection are discussed in Sect. 4. Section 5 describes the summary and conclusion.

2 Data

The monthly precipitation and SST fields from the historical simulations of 32 climate models from CMIP5 database are used. The twentieth century historical climate simulations are forced by observed atmospheric composition changes that reflect both natural (volcanic influences, solar forcing, aerosols, and emissions of short-lived species and their precursors) and anthropogenic components (i.e., GHGs and AAs) as well as time-varying estimates of land cover (Taylor et al. 2012). The list of 32 CMIP5 models

Table 1 List of CMIP5 models along with their modeling groups and resolution

Model	Institution	Resolution (latitude × longitude)
BCC-CSM1-1	Beijing Climate Center, China Meteorological Administration, China	64 × 128
BCC-CSM1-1-m	Beijing Climate Center, China Meteorological Administration, China	160 × 320
BNU-ESM	College of Global Change and Earth System Science, Beijing Normal University, China	64 × 128
CCSM4	National Center for Atmospheric Research, USA	192 × 288
CMCC-CESM	Centro Euro-Mediterraneo per I Cambiamenti Climatici, Italy	48 × 96
CMCC-CMS	Centro Euro-Mediterraneo per I Cambiamenti Climatici, Italy	96 × 192
CanCM4	Canadian Centre for Climate Modelling and Analysis, Canada	64 × 128
CanESM2	Canadian Centre for Climate Modelling and Analysis, Canada	64 × 128
GFDL-CM3	Geophysical Fluid Dynamics Laboratory, USA	90 × 144
GFDL-ESM2G	Geophysical Fluid Dynamics Laboratory, USA	90 × 144
GFDL-ESM2M	Geophysical Fluid Dynamics Laboratory, USA	90 × 144
GISS-E2-H	NASA Goddard Institute for Space Studies, NY	90 × 144
GISS-E2-R	NASA Goddard Institute for Space Studies, NY	90 × 144
HadCM3	Met Office Hadley Centre, UK	73 × 96
HadGEM2-AO	National Institute of Meteorological Research/Korea Meteorological Administration, South Korea	145 × 192
HadGEM2-CC	Met Office Hadley Centre, UK	145 × 192
HadGEM2-ES	Met Office Hadley Centre, UK	145 × 192
INM-CM4	Institute for Numerical Mathematics, Russia	120 × 180
IPSL-CM5A-LR	Institut Pierre-Simon Laplace, France	96 × 96
IPSL-CM5A-MR	Institut Pierre-Simon Laplace, France	143 × 144
IPSL-CM5B-LR	Institut Pierre-Simon Laplace, France	96 × 96
MIROC4h	Atmosphere and Ocean Research Institute (The University of Tokyo), National Institute for Environmental Studies, and Japan Agency for Marine-Earth Science and Technology, Japan	320 × 640
MIROC5	Atmosphere and Ocean Research Institute (The University of Tokyo), National Institute for Environmental Studies, and Japan Agency for Marine-Earth Science and Technology, Japan	128 × 256
MIROC-ESM	Japan Agency for Marine-Earth Science and Technology, Atmosphere and Ocean Research Institute (The University of Tokyo), and National Institute for Environmental Studies, Japan	64 × 128
MIROC-ESM-CHEM	Japan Agency for Marine-Earth Science and Technology, Atmosphere and Ocean Research Institute (The University of Tokyo), and National Institute for Environmental Studies, Japan	64 × 128
MPI-ESM-LR	Max Planck Institute for Meteorology (MPI-M), Germany	96 × 192
MPI-ESM-MR	Max Planck Institute for Meteorology (MPI-M), Germany	96 × 192
MPI-ESM-P	Max Planck Institute for Meteorology (MPI-M), Germany	96 × 192
MRI-CGCM3	Meteorological Research Institute, Japan	160 × 320
MRI-ESM1	Meteorological Research Institute, Japan	160 × 320
NorESM1-M	Norwegian Climate Centre, Norway	96 × 144
NorESM1-ME	Norwegian Climate Centre, Norway	96 × 144

under consideration and their pertinent information is provided in Table 1. For each model, the first ensemble member (i.e., r1i1p1) run has been used and the analysis is generally carried out for the period 1901–2004 for all models, except CanCM4 (1961–2004) and MIROC4h (1950–2004). More details on models and experiments can be found in Taylor et al. (2012). All model outputs are freely accessible at http://esgf-index1.ceda.ac.uk maintained by Earth System Grid Federation (ESGF).

To scrutinize the observed IPO and its impacts on Indian rainfall, the monthly SST data from the U.K. Met office's Hadley Centre Sea Ice and Sea Surface Temperature dataset, version 1.1 (HadISST 1.1; Rayner et al. 2003) and the precipitation from Climatic Research Unit time series version 3.22 (CRU TS3.22; Harris et al. 2014) for the period 1901–2004 are used. For assessing CMIP5 model's fidelity in simulating the rainfall climatology and seasonal cycle, the monthly precipitation dataset from the Global

Precipitation Climatology Project (GPCP version 2.2, Huffman et al. 2009) for the period 1979–2004 is used.

To examine the large-scale features associated with IPO, the National Center for Environmental Prediction (NCEP)/ National Center for Atmospheric Research (NCAR) atmospheric reanalysis V1 (Kalnay et al. 1996) monthly data for zonal (u), meridional (v) wind, and sea level pressure (SLP) for the period 1948–2004 are obtained from http://www. esrl.noaa.gov/psd/data/gridded/data.ncep.reanalysis.html. The resolution of each model dataset differs, therefore, for ease of comparison all model outputs as well as observational data are interpolated into common latitude-longitude grid (2.5° × 2.5°) by bilinear interpolation.

3 Method of analysis

Firstly, the annual mean SSTAs have been computed. The computed annual mean SSTAs are then smoothened by applying 3-year moving average to reduce the influence of interannual variability on the shape of pattern, thereafter the obtained field is detrended to remove the global component of the anthropogenic forcing. The unfiltered IPO index from observation is then defined as the first principal component (PC-1) of the detrended smoothed annual mean SSTAs, allied to the first empirical orthogonal function (EOF-1) computed over the Pacific basin (45°S–60°N, 140°E–80°W). As reported in many previous studies (Zhang et al. 1997; Dai 2013; Dong and Dai 2015), the "horse-shoe" shape of this EOF (i.e., EOF-1; Fig. 13a) exhibits ENSO-like SST patterns in the Pacific basin (Alexander et al. 2002) and PDO like SST patterns in the North Pacific (Mantua et al. 1997). Thus, Fig. 13a clearly suggests that the PDO is a part of the IPO that extends to the whole Pacific basin. The temporal coefficient (i.e., PC-1; Fig. 13b) contains both ENSO-related multi-year variations as well as decadal-to-multidecadal variations.

Since the focus of the present study is to examine the IPO-ISMR teleconnection on multidecadal basis, the obtained unfiltered IPO index is filtered using Butterworth low-pass filter of order 4 and cut-off frequency 21-year (shown by red line; Fig. 13b). It should be noted that due to the end effects of low-pass filter, there is an uncertainty in defining the low-pass filtered time series at the ends; therefore, the first and last 10-points of the filtered time series are ignored in the analysis (Joshi and Rai 2015). Thus, our analysis focuses mainly on the multidecadal variations from the entire Pacific, in contrast to many previous studies (e.g., Zhang et al. 1997; Power et al. 1999; Krishnan and Sugi 2003; Meehl et al. 2013), in which most decadal (10–20 year) variations were often retained. The low-pass filtered IPO indices for the forced simulations are also derived using the same methodology as discussed above.

In the present study, the methodology adopted to derive IPO is very similar to the one used in Dai (2013) as well as Dong and Dai (2015), with the difference that they do not de-trend the data prior to perform EOF analysis and consider therefore second EOF (EOF-2) as IPO. Further, it has been verified that the observed EOF-1 and PC-1 of our analysis (Fig. 13) are very consistent to EOF-2 and PC-2 shown as Fig. 1 in Dai (2013) as well as Dong and Dai (2015).

4 Results and discussion

Before examining the IPO-ISMR teleconnection in the CMIP5 models, it is essential to assess the model's fidelity in simulating the precipitation over the Indian domain as well as the IPO related SST pattern over the Pacific basin.

4.1 Simulation of the rainfall in CMIP5 models

The capability of CMIP5 models in simulating the precipitation is assessed through the use of two Taylor diagrams (Taylor 2001), based on the fidelity in simulating the annual cycle that represents the climatological monthly mean of precipitation area-averaged over the monsoon core region (10°N–30°N, 70°E–100°E) and the spatial pattern of climatological seasonal, i.e., June–September (JJAS) mean rainfall over the Indian monsoon region (15°S–30°N, 50°E–120°E).

Taylor diagrams are well accepted performance metrics for climate models that provide a succinct statistical outline of how well the spatial/temporal patterns match each other in terms of their correlation coefficients (CCs), their root-mean-square error (RMSE), and the simulated to observed ratio of their variances. The distance from the origin specifies the standardized deviation of each model, i.e., the distance from the origin is the standard deviation (SD) of the model, normalized by the SD of the observation. If the SD of model is same as that of the observation, then the radius will be 1. The distance from the reference point to the plotted point gives the RMSE. The closer the plotted point to the reference point, the smaller will be the RMSE. The correlation between the model and the observation is the cosine of the polar angle. If the correlation between the model and observation is 1, then the point will lie on the horizontal axis. Using this metric, the models having the highest CC, standardized deviation close to the unity (i.e., close to the observation), and smaller RMSE are considered to be the best.

Figure 1 shows the fidelity of each model to simulate the annual cycle that represents the climatological monthly mean of precipitation area-averaged over the monsoon core region. Except IPSL-CM5B-LR and IPSL-CM5A-LR, all
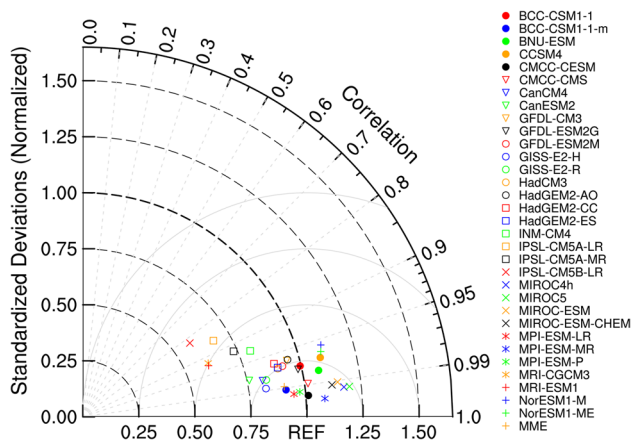
Fig. 1 Taylor diagram of the annual cycle, representing the climatological monthly mean of precipitation area-averaged over the monsoon core region (10°N–30°N, 70°E–100°E), simulated in the CMIP5 models. The monthly GPCP data is used as a reference data
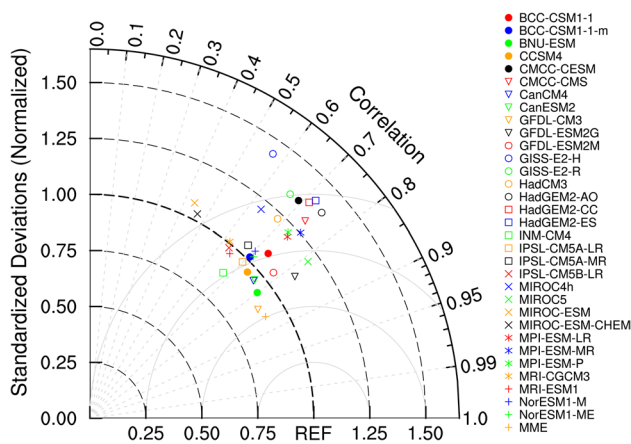

Fig. 2 Taylor diagram of the spatial pattern of climatological seasonal (JJAS) mean precipitation simulated in the CMIP5 models over the Indian monsoon region (15°S–30°N, 50°E–120°E). The monthly GPCP data is used as a reference data

other models show a correlation value greater than 0.9. Although these 30 models exhibit large correlations, some underestimate or overestimate the variance. In terms of both magnitude and phase, the models BCC-CSM1-1, CMCC-CESM, CMCC-CMS, GFDL-ESM2G, MPI-ESM-LR, MPI-ESM-MR, and MPI-ESM-P are very close to the observation (Fig. 1) and hence, simulate the best annual cycle as compared to other models.

The Taylor diagram, shown in Fig. 2, depicts the model's fidelity to simulate the spatial pattern of climatological seasonal (JJAS) mean rainfall over the Indian monsoon region. The majority of models show good correlations, but some of them either underestimate or overestimate the spatial variance. The models BNU-ESM, GFDL-CM3, GFDL-ESM2G, and MIROC5 have largest correlation in terms of

simulating the spatial pattern of climatological seasonal mean precipitation. However, BNU-ESM and GFDL-CM3 slightly underestimate the spatial variance, while the remaining two overestimate it. To identify models that can simulate a reasonable spatial pattern of climatological seasonal mean precipitation compared to other models, we defined a criterion CC > 0.6 and normalized SD lying between 0.75 and 1.25. Based on this criterion, the models MIROC-ESM and MIROC-ESM-CHEM have lowest correlation, while the models GISS-E2-H, GISS-E2-R, CMCC-CESM, CMCC-CMS, HadGEM2-AO, HadGEM2-CC, HadGEM2-ES, and MPI-ESM-MR are highly overestimating the climatological seasonal mean precipitation. The models are not selected based on the above criterion for the analysis of the IPO-ISMR teleconnection, because all models are to some extent able to reproduce the ISMR seasonal cycle and climatology. Also, a selection would involve the risk of excluding models from further analysis because of ad-hoc and subjectively chosen thresholds.

4.2 Simulation of the IPO in CMIP5 models

Figure 3 shows the regression maps of annual SSTAs onto the normalized low-pass filtered IPO index for observation and CMIP5 models. The sign convention is such that the IPO index is taken as positive if the mean tropical Pacific SSTAs are positive as observed in the regression maps (otherwise the index is multiplied by −1). It is clearly seen that most of the models show well defined spatial pattern of IPO over the Pacific basin having warm SSTAs in the tropical Pacific as well as in the north and south of the eastern part of the basin and cold SSTAs in the western part of the basin, poleward of 25° and more protuberant in the Northern Hemisphere, except BCC-CSM1-1, CCSM4, GFDL-CM3, GFDL-ESM2G, GFDL-ESM2M, GISS-E2-R, HadGEM2-AO, HadGEM2-CC, HadGEM2-ES, IPSL-CM5B-LR, MIROC-ESM, and MPI-ESM-MR. These CMIP5 models poorly represent the spatial pattern of IPO and amongst these GFDL-CM3, GFDL-ESM2G, GISS-E2-R, HadGEM2-AO, and IPSL-CM5B-LR show strong positive SSTAs over the western Pacific basin poleward to 25°N. The models GISS-E2-H, MIROC5, and MRI-CGCM3 show weak positive SSTAs over the tropical Pacific. It should be noted that the spatial structures of GFDL-CM3, GFDL-ESM2G, HadGEM2-AO, and MIROC-ESM do not look very IPO-like and appear as an overall warming pattern. On verifying the time series of their first PCs, it is observed that they do have decadal variations (figure not shown). Further, on scrutinizing the regression patterns of annual SSTAs onto the normalized low-pass filtered second PCs for these models, it is observed that the resulting structures appear even less IPO-like (figure not shown) as compared to the ones derived
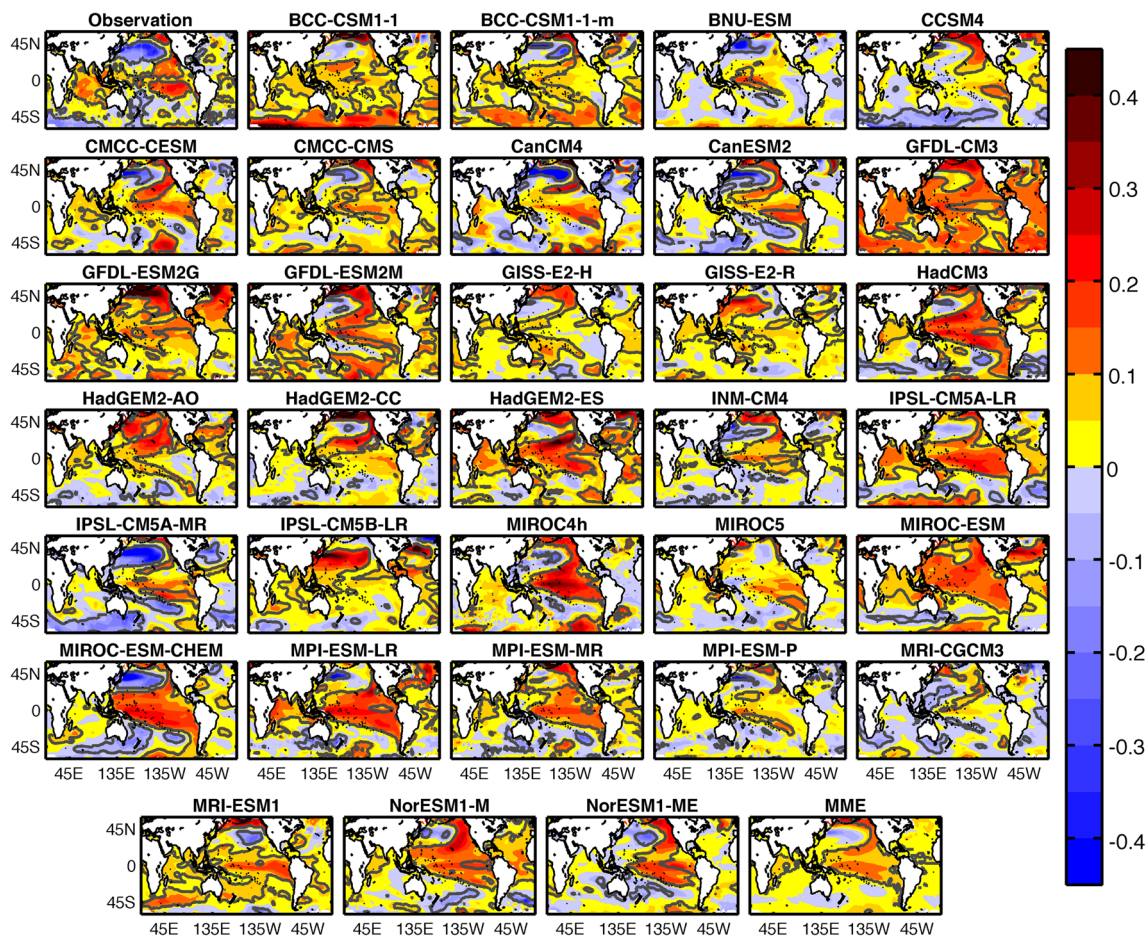
Fig. 3 Regression maps of annual SSTAs onto the standardized low-pass filtered IPO index (units are °C per standard deviation) for observation and 32 CMIP5 models. The *grey contours* in observation and CMIP5 models indicate the regions where the regression coefficient is statistically significant at 95 % confidence level, which is assessed via a two-tailed *t* test; whereas in MME (computed by averaging across all models) it indicate the regions where the regression coefficient coincides in at least 28 out of the 32 models considered

from first PCs. In order to test the robustness of results, all analyses from the following sections are repeated without including the above-mentioned four models (figures not shown), and the results are very similar to the ones presented in this study. Thus, the results are not sensitive to the exclusion or inclusion of these models. The multi-model ensemble (MME; computed by averaging across all models) also shows an explicit spatial pattern of IPO, which is quite consistent with observation, although smaller in magnitude because of averaging across models. Consistent with observation, most of the models show warming over the Indian and Atlantic Oceans, except BNU-ESM, CCSM4, and MRI-CGCM3. These models show cooling over the Indian Ocean. The robustness of the result shown in Fig. 3 is also tested for different cut-off frequencies like 15-, 17- and 19-year. The results are in good agreement with the one reported in Fig. 3.

The overall fidelity of each model to simulate the spatial pattern of IPO over the Pacific basin is also assessed using

Taylor Diagram Metric (Taylor 2001). Taylor diagram of spatial regression coefficients obtained by regressing annual SSTAs onto the normalized low-pass filtered IPO index over the Pacific basin (Fig. 4) shows negative correlation for the models like IPSL-CM5B-LR, HadGEM2-AO, GISS-E2-R, and GISS-E2-H, which is consistent from Fig. 3, while the models like MRI-CGCM3, GFDL-ESM2G, and GFDL-CM3 show weak, but positive correlation. Out of 32 CMIP5 models under consideration, more than 50 % models show good correlation, but some of them either underestimate or overestimate the spatial variance (Fig. 4). The models IPSL-CM5A-MR, MIROC-ESM-CHEM, CanCM4, and CMCC-CMS have highest correlation in terms of simulating the spatial pattern of IPO. However, the first three highly overestimate the spatial variance, while the last highly underestimates it. The correlation in case of MME is fairly good, i.e., around 0.7, but it highly underestimates the spatial variance. The models having CC > 0.4 and SD lying between 0.75 and 1.25 are good

in simulating the spatial pattern of IPO. Considering the variance part, BCC-CSM1-1-m, CMCC-CESM, and MPI-ESM-LR are the best models.
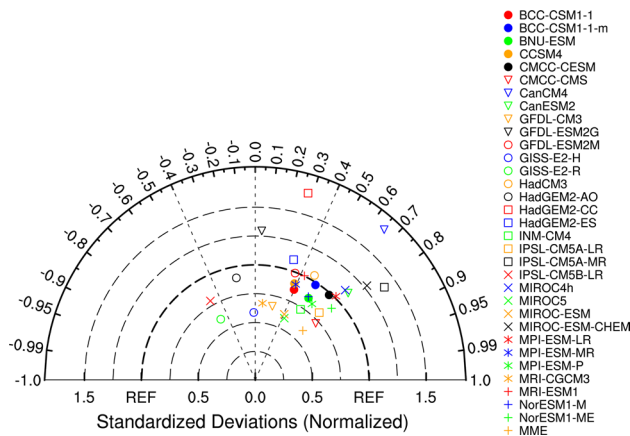

Fig. 4 Taylor diagram of the spatial regression coefficients obtained by regressing annual SSTAs onto the standardized low-pass filtered IPO index over the Pacific basin (45°S–60°N, 140°E–80°W)
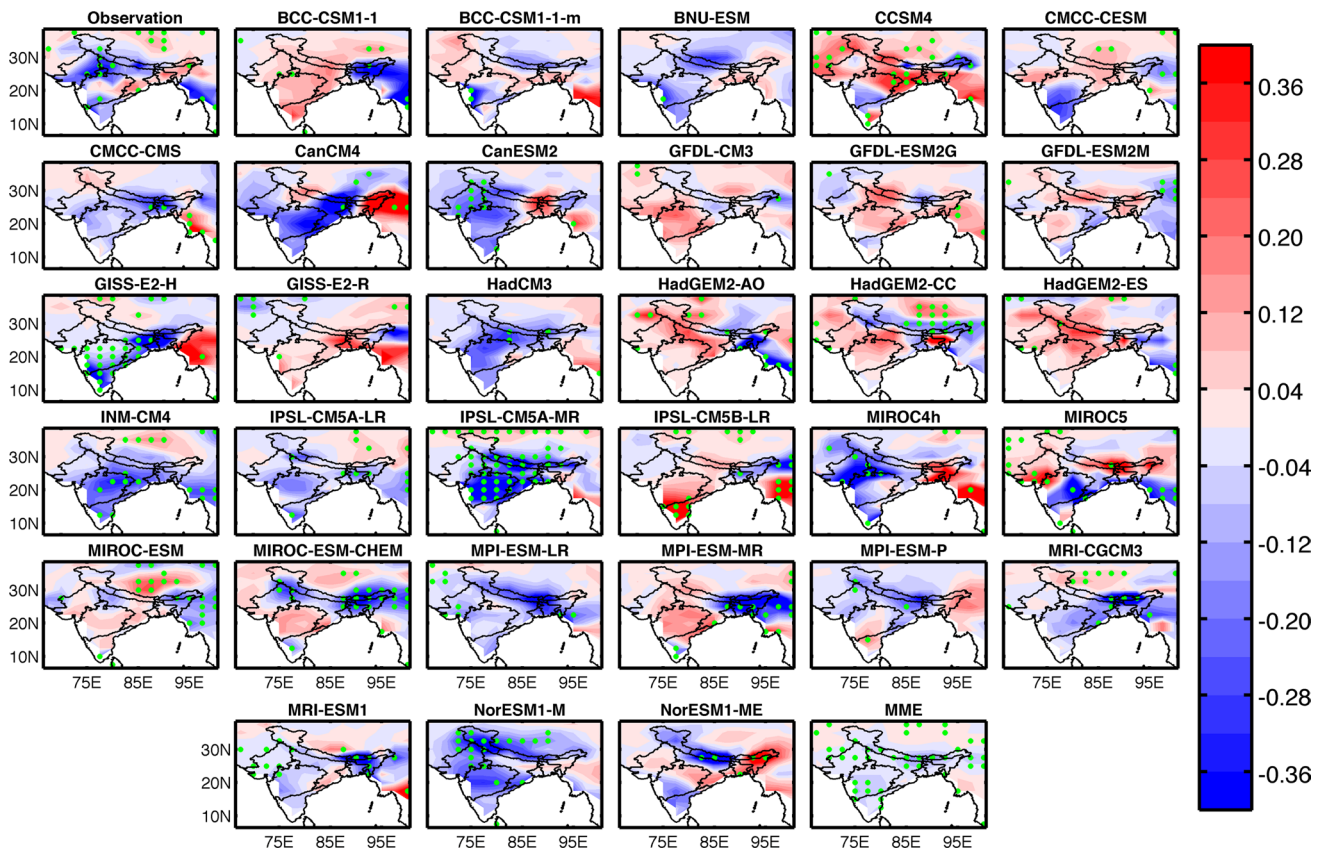
4.3 IPO-ISMR teleconnection

In order to assess the model's fidelity in representing the IPO-ISMR teleconnection, the JJAS precipitation anomalies are regressed onto the normalized low-pass filtered IPO Index (Fig. 5). The observed regression pattern shows negative anomalies over most parts of India, except northeast region. This regression pattern is fairly consistent with Fig. 4a of Joshi and Rai (2015) in which the India Meteorological Department (IMD) gridded rainfall data (Rajeevan et al. 2008) is used for computing the correlation map between low-pass filtered IPO and rainfall. The regression pattern of most models shows negative anomalies over all-India, except BCC-CSM1-1, CCSM4, GFDL-CM3, GFDL-ESM2G, GFDL-ESM2M, GISS-E2-R, HadGEM2-AO, HadGEM2-CC, HadGEM2-ES, IPSL-CM5B-LR, MIROC-ESM, and MPI-ESM-MR. Amongst these, the first five CMIP5 models reasonably simulate the climatological seasonal mean rainfall, but fail to represent the IPO related spatial pattern; whereas, the rest neither simulates the rainfall well nor the IPO related spatial pattern. It is

Fig. 5 Regression maps of JJAS precipitation anomalies onto the standardized low-pass filtered IPO index (units are mm/d per standard deviation) for observation and 32 CMIP5 models. The green stippling in observation and CMIP5 models indicates the grid point where the regression coefficient is statistically significant at 90 % confidence level, which is assessed via a two-tailed *t* test; whereas in MME it depicts the grid point where the sign of regression coefficient coincides in at least 20 out of the 32 models considered
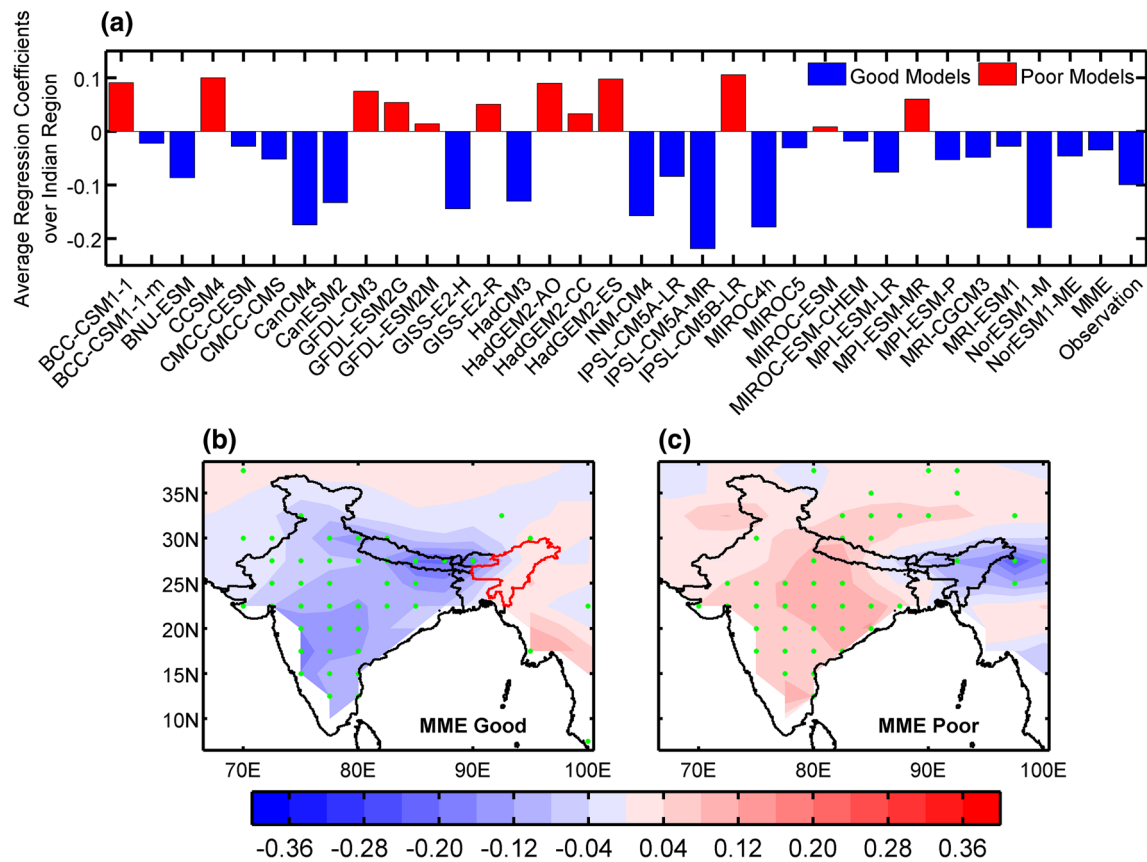
Fig. 6 a Area average of the IPO precipitation regression maps (shown in Fig. 5) over Indian land points (i.e., area enclosed within the black boundary shown in **b**), excluding northeast region (i.e., area enclosed within the *red boundary* shown in **b**). CMIP5 model's having negative (positive) average regression coefficient is categorized as good (poor) model shown by *blue* (*red*) *bar* in **a**. **b**, **c** Ensemble means of the IPO precipitation regression patterns of 20 good (MME good) and 12 poor (MME poor) CMIP5 models, respectively. The green stippling in MME good and MME poor indicates the grid point where the sign of regression coefficient coincides in at least 15 out of the 20 good and 9 out of the 12 poor models, respectively. The unit of regression coefficient is mm/d per standard deviation

also seen that the models BNU-ESM, CanCM4, CanESM2, MIROC4h, and NorESM1-M show the best regression pattern as seen in the observation, i.e., the negative anomalies over most parts of India and the positive anomalies over northeast region, which signifies that the warm phase of IPO causes decrease in rainfall over all-India, while it causes enhancement of rainfall over northeast region and vice versa. It should be noted that the time span of models CanCM4 and MIROC4h are relatively short for assessing the IPO-ISMR teleconnection, but these models are amongst those which are showing the best regression patterns. So the purpose of including these models is to inform the modeling communities that the long runs of these models will be more beneficial for further studies. The MME fails to represents the IPO-ISMR teleconnection over northeast region, while over rest of India it is quite consistent with observation.

Figure 6a depicts the area average of each regression map shown in Fig. 5 over Indian land points (i.e., area enclosed within the black boundary shown in Fig. 6b),

excluding northeast region (i.e., area enclosed within the red boundary shown in Fig. 6b). It is observed that approximately two-thirds of the models show negative average regression coefficients over all-India. The models for which the average regression coefficient is positive are the ones that are generally showing the poor spatial pattern of IPO, regardless of the extent to which they reproduce the precipitation climatology or seasonal cycle. In order to support the above statement, a scatter plot between the IPO precipitation regressions averaged over Indian land points, excluding northeast region and CCs (shown in Fig. 4) representing the fidelity of CMIP5 models to simulate the IPO patterns is computed (Fig. 14). The resulting relation is strong (−0.574) and statistically significant, indicating that the models that are capable of simulating the spatial pattern of IPO also produces stronger negative Indian land rainfall responses. This scatter plot clearly depicts that in general the IPO-ISMR teleconnection does not hold for the models, which are poorly simulating the spatial pattern of IPO.

Fig. 7 Ensemble means of the IPO SST regressions of **a** good (MME good) and **b** poor (MME poor) CMIP5 models, which are computed by averaging the regression maps of annual SSTAs onto the standardized low-pass filtered IPO index (shown in Fig. 3) across all 20 good and 12 poor models that are shown by *blue* and *red bars* in Fig. 6a, respectively. The green stippling in MME good and MME poor indicates the grid point where the sign of regression coefficient coincides in at least 15 out of the 20 good and 9 out of the 12 poor models, respectively. The unit of regression coefficient is °C per standard deviation
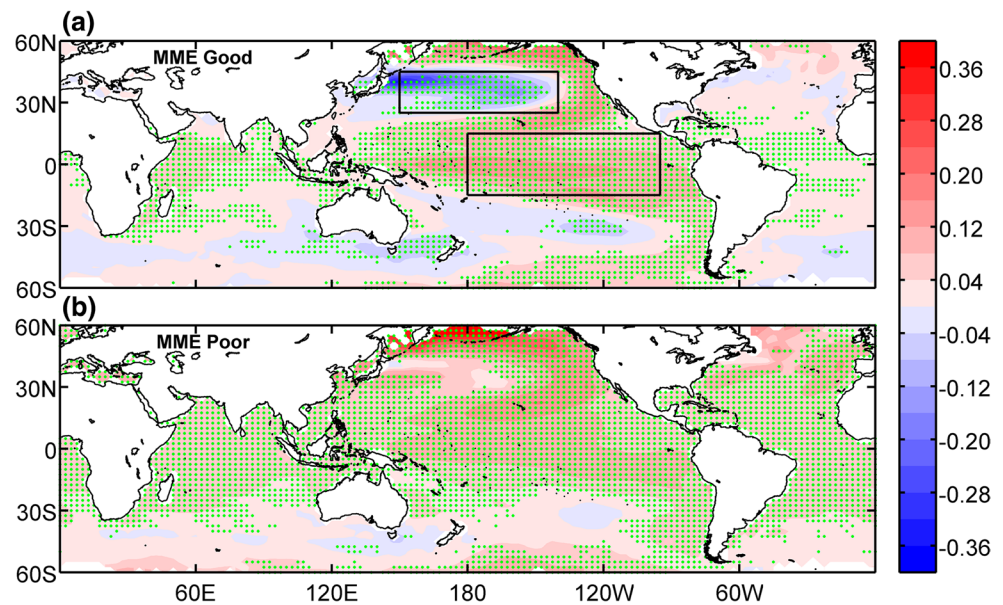
Based on the sign of average regression coefficients, the models are categorized into two groups (1) good (having negative average regression coefficients; shown by blue bars in Fig. 6a) and (2) poor (having positive average regression coefficients; shown by red bars in Fig. 6a). Following this criterion, 20 models (BCC-CSM1-1-m, BNU-ESM, CMCC-CESM, CMCC-CMS, CanCM4, CanESM2, GISS-E2-H, HadCM3, INM-CM4, IPSL-CM5A-LR, IPSL-CM5A-MR, MIROC4h, MIROC5, MIROC-ESM-CHEM, MPI-ESM-LR, MPI-ESM-P, MRI-CGCM3, MRI-ESM1, NorESM1-M, and NorESM1-ME) are identified as good and 12 models (BCC-CSM1-1, CCSM4, GFDL-CM3, GFDL-ESM2G, GFDL-ESM2M, GISS-E2-R, HadGEM2-AO, HadGEM2-CC, HadGEM2-ES, IPSL-CM5B-LR, MIROC-ESM, and MPI-ESM-MR) are identified as poor. The ensemble mean of the IPO precipitation regression maps of 20 good models (MME good; Fig. 6b) closely resembles the observation (observed regression pattern; Fig. 5), i.e., showing negative anomalies over all-India and positive anomalies over most parts of northeast region, whereas the ensemble mean of 12 poor models (MME poor; Fig. 6c) shows a reverse pattern. Model like GISS-E2-H represents reasonably well the IPO-ISMR teleconnection as compared to observation, even though this model is highly overestimating the climatological seasonal mean rainfall (Fig. 2) and also showing weak positive SSTAs over the tropical Pacific (Fig. 3) as well as the Taylor diagram of spatial regression coefficients, obtained by regressing annual SSTAs onto the standardized low-pass filtered IPO index over the Pacific basin, also reveals feeble negative correlation (Fig. 4). On the other hand, MIROC-ESM-CHEM and CMCC-CESM show well-defined spatial structure of the IPO (Fig. 3) having a CC of 0.77 and 0.66

as compared to observation (Fig. 4), but the impact of IPO on rainfall for these models is very weak, though negative (Fig. 6a). This may be due to the fact that these models are not simulating the climatological seasonal mean rainfall well. MIROC-ESM-CHEM is showing weak correlation with observed climatological seasonal mean precipitation having a CC 0.47; whereas, CMCC-CESM is highly over-estimating the rainfall (Fig. 2).

This result raises the question if there is any relation between the quality of reproducing IPO and the IPO-ISMR teleconnection in the models. In order to get further insight into the crucial elements in the modeled IPO pattern, the ensemble means of the IPO SST regressions of good (MME good; Fig. 7a) and poor (MME poor; Fig. 7b) models are computed by averaging the regression maps of annual SSTAs onto the standardized low-pass filtered IPO index (shown in Fig. 3) across all 20 good and 12 poor models shown by blue and red bars in Fig. 6a, respectively. Clearly, a striking feature of the good model's composite is the pronounced tropical–extratropical SST gradient of the IPO regression pattern, which compares well with the observations (observed IPO SST regression in Fig. 3). On the other hand, the poor models show a weak tropical–extratropical SST gradient. This result suggests to use the tropical–extratropical gradient in the IPO SST regression as a parameter. Figure 8a shows the scatter plot of the mean regression coefficient of precipitation over Indian land points and the difference of tropical Pacific (15°S–15°N, 180°E–95°W) and extratropical Pacific (25°N–45°N, 150°E–140°W) SSTAs in the IPO regressions of the models. There is a strong and 95 % statistically significant negative correlation (−0.66) between the tropical–extratropical SST gradient in the IPO regressions and the mean Indian land rainfall
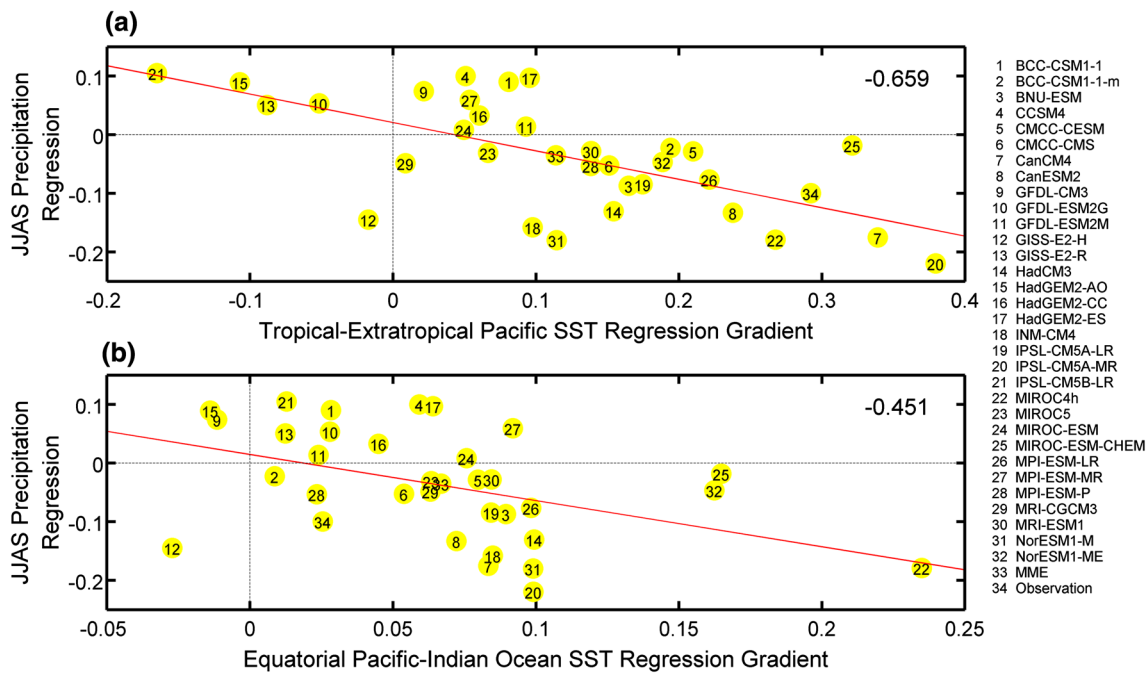
Fig. 8 Scatter plot of the IPO precipitation regressions (units are mm/d per standard deviation) averaged over Indian land points, excluding northeast region versus the difference between mean IPO SST regressions (units are °C per standard deviation) over **a** the tropical (15°S–15°N, 180°E–95°W, box over the tropical Pacific in Fig. 7a) and extratropical (25°N–45°N, 150°E–140°W, box over the extratropical Pacific in Fig. 7a) Pacific Ocean and **b** the Niño 3.4 (5°S–5°N, 120°W–170°W) region and Indian Ocean (10°S–10°N, 60°E–90°E)

IPO regressions. This indicates that models with larger tropical–extratropical IPO SST regression gradient also produce larger negative Indian land rainfall responses. It is also worth noting that the observation is quite close to the regression line, indicating that models which have a correct tropical–extratropical IPO SST regression gradient also produce an ISMR response that is close to the observed. This result is consistent with Feudale and Kucharski (2013), who also identified the tropical–extratropical SST gradient most important feature of the global SST pattern responsible for common multidecadal African and Indian rainfall variability. Such an SST gradient also leads to a surface pressure gradient change in the Indian Ocean region that modifies the ISMR. Since the ensemble means of the IPO SST regressions of good and poor models also show differences over the Indian Ocean, therefore, a scatter plot between the IPO precipitation regressions averaged over Indian land points, excluding northeast region and the IPO SST regressions averaged over the Indian Ocean (10°S–10°N, 60°E–90°E) is computed (figure not shown). The resulting correlation is rather weak (0.23) and not statistically significant.

Figure 7 suggests that several other features of the differences between the SST pattern for good and poor models may also be relevant. Therefore, several other scatter plots have also been considered, for example, the IPO precipitation regressions averaged over Indian land points

as in Fig. 8a versus (a) the IPO SST regressions averaged over Niño 3.4 (5°S–5°N, 120°W–170°W; figure not shown) region, (b) the IPO SST regressions averaged over Niño 4 (5°S–5°N, 160°E–150°W; figure not shown) region, and (c) the difference between mean IPO SST regressions over Niño 3.4 region and Indian Ocean as shown in Fig. 8b. For the first two scatter plots, the correlation is rather weak (-0.28 and -0.25, respectively), and not statistically significant. For the latter one the correlation becomes stronger (-0.45) and is statistically significant, but still much smaller than for the tropical–extratropical Pacific SST gradient. It is therefore possible that the tropical–extratropical Pacific SST gradient is the most important feature for the good models, with some contribution also from the zonal equatorial Pacific-Indian Ocean SST gradient.

4.4 Atmospheric circulation, velocity potential, and sea level pressure associated with the IPO

In order to investigate the atmospheric circulation pattern associated with the IPO, the JJAS zonal and meridional wind anomalies (from NCEP/NCAR reanalysis) at 850 hPa and the annual SSTAs are regressed onto the normalized low-pass filtered IPO index for the period 1948–1993. The IPO SST regression pattern for the period 1948–1993 (figure not shown) is quite consistent with the one obtained for

Fig. 9 a Regression of JJAS seasonal anomalies of zonal and meridional winds at 850 hPa (plotted as vectors) from NCEP/NCAR reanalysis (1948–1993) onto the standardized low-pass filtered IPO index. **b, c** Same as in **a**, but for the averaged regressions of 20 good and 12 poor CMIP5 models, respectively. Magnitude of winds is represented by *shaded color* and vectors represent wind direction. The unit of wind is m/s per standard deviation
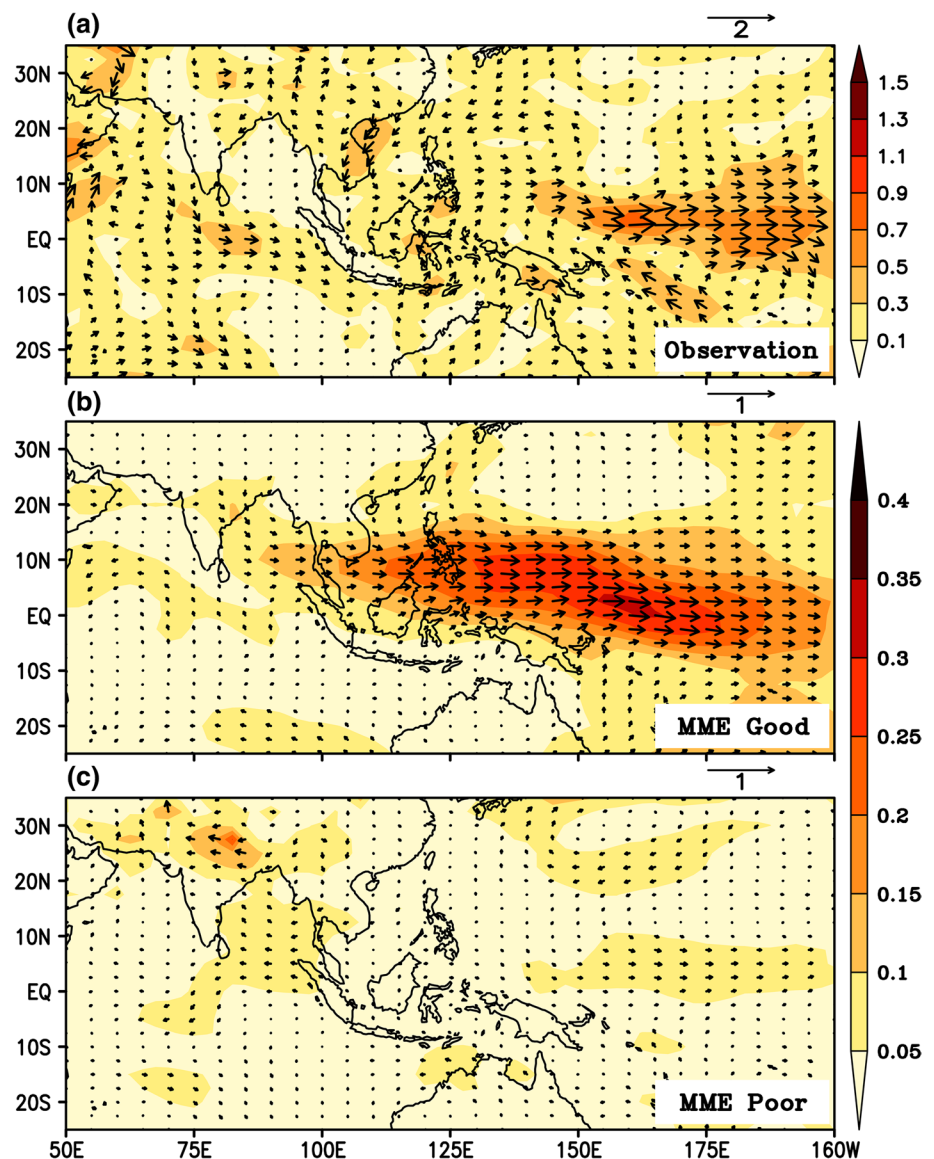

the period 1912–1993 (observed IPO SST regression pattern; Fig. 3), i.e., exhibiting positive SSTAs over the tropical Pacific and negative over the extratropics (poleward of 25°), especially in the northern Pacific sector. This indicates that the wind circulation pattern shown in Fig. 9a is linked with the warm phase of IPO.

The observed regression pattern of winds (850 hPa) depicts that the positive SSTAs in the tropical Pacific are allied with westerly anomalies along the equator. This is in agreement with the findings of Joshi and Rai (2015) who reported that the easterlies in the equatorial Pacific are strengthened during the cold phase of IPO as compared to its warm phase. The regression pattern also reveals that during the warm phase of IPO the winds are blowing away from the continent into the Arabian Sea, reducing the moisture flow over India, which is consistent with the drought condition.

Wang et al. (2013) stated that the warming in the eastern Pacific and cooling in the western Pacific will weaken the easterly trade winds that will cause the divergence of moisture from the Asian and African monsoon regions, which in turn decrease the Northern Hemisphere summer monsoon (NHSM) rainfall and vice versa. Meehl and Hu (2006) also proposed that the warm phase of IPO is characterized with relatively warm tropical SSTs, positive convective precipitation and convective heating anomalies in the tropical Pacific, weak trade winds and subtropical cells that will produce multidecadal drought like conditions over the extended Indian monsoon region and anomalously wet conditions over the Great Basin region in the southwestern United States.

Figure 9b, c show the composites of the IPO wind regressions for good and poor CMIP5 models, respectively. The composite of good models shows westerly anomalies

Fig. 10 a Regression of JJAS anomaly of velocity potential at 850 hPa from NCEP/NCAR reanalysis (1948–1993) onto the standardized low-pass filtered IPO index. **b, c** Same as in Fig. 10a, but for the averaged regressions of 20 good and 12 poor CMIP5 models, respectively. The unit of velocity potential is 10^6 m^2/s per standard deviation. The vectors represent the divergent wind (m/s)
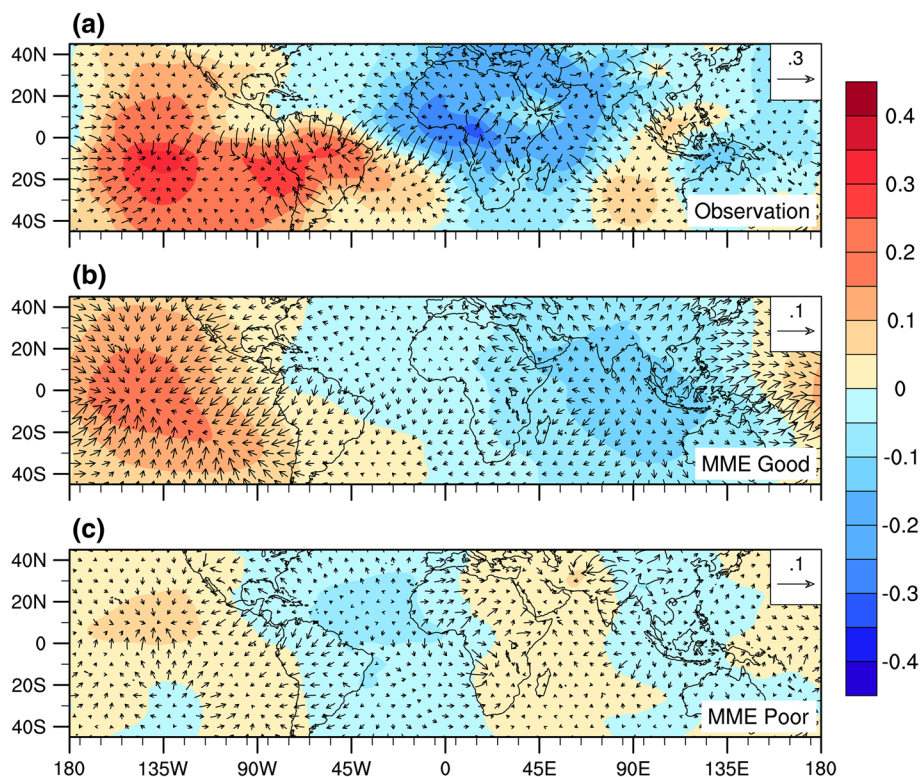
along the equator, which are slightly weaker in magnitude as compared to observation (Fig. 9a). On the other hand, the poor model's composite also shows westerly anomalies, but of very small magnitude as compared to observed regression pattern (Fig. 9a). The composite of IPO wind regressions for good models also divulges that the winds are blowing away from the Indian subcontinent, though the pattern seems to be shifted substantially towards the northeast with respect to observation. Nevertheless, the IPO wind regression of good models is also indicating the lack of moisture over India, which is consistent with the drought condition. On the contrary, the poor models completely fail to represent the circulation pattern over the Indian subcontinent.

The atmospheric general circulation is basically characterized by flows in the lower as well as in the upper troposphere. In general, the convergence (divergence) at lower level typically coincides with divergence (convergence) at upper level that strongly indicates the large-scale monsoonal overturning circulations. Velocity potential is a measure of divergent flow and is often used as a proxy for the Walker circulation. At upper level, a region of negative (positive) potential has diverging (converging) winds, which exemplifies strong convection (subsidence), i.e., rising (sinking) motion at lower level.

Figure 10a (Fig. 11a) shows the regression of the unfiltered JJAS anomaly of velocity potential at 850 hPa

(150 hPa) from NCEP/NCAR reanalysis (1948–1993) onto the standardized low-pass filtered IPO index. Figure 10a depicts that the warm phase of IPO is associated with anomalous convergence (i.e., positive potential) over the central tropical Pacific as well as over the Southwest United States [in accordant with the findings of Dai (2013)] and divergence over West Africa [in agreement with the findings of Villamayor and Mohino (2015)] as well as over the extended Indian monsoon region at low levels and with anomalous divergence and convergence over the respective regions at high levels (Fig. 11a).

The anomalous convergence at low levels over the central tropical Pacific is consistent with the eastern Pacific warming signal that indicates anomalous Walker cell, i.e., the weakening of zonal overturning circulation. Because of the subsidence, the atmosphere over the western end of Pacific is highly stable, which is unfavorable to and limits the occurrence of deep clouds and precipitation. In contrast, over the eastern–central tropical Pacific the atmosphere is unstable and deep convective clouds and heavy precipitation will occur frequently. This anomalous circulation reduces the easterly trade winds across the tropical Pacific in the lower atmosphere, which is clearly distinct in the observed winds regression pattern at 850 hPa (Fig. 9a). On the other hand, this anomalous circulation also weakens the westerly winds across the tropical Pacific in the upper atmosphere (figure not shown). This is in agreement with

Fig. 11 a Regression of JJAS anomaly of velocity potential at 150 hPa from NCEP/NCAR reanalysis (1948–1993) onto the standardized low-pass filtered IPO index. **b, c** Same as in **a**, but for the averaged regressions of 20 good and 12 poor CMIP5 models, respectively. The unit of velocity potential is $10^6 \, m^2/s$ per standard deviation. The vectors represent the divergent wind (m/s)
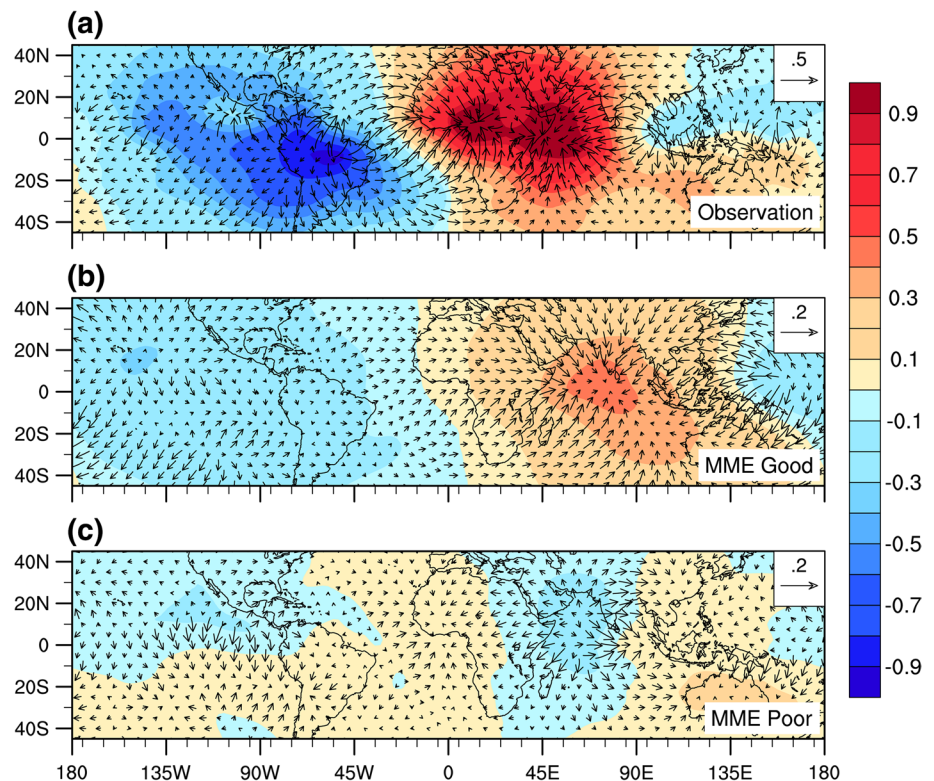
Krishnamurthy and Krishnamurthy (2014) who proposed a mechanism that the warm phase of IPO-like variability affects the equatorial trade winds, which in turn weakens the equatorial Walker circulation that leads to enhanced ascending motion in the central Pacific and descending motion over the Maritime Continent.

Figure 10b, c (Fig. 11b, c) show the averaged regressions of the unfiltered JJAS anomaly of velocity potential at 850 hPa (150 hPa) for good and poor CMIP5 models, respectively. The regression pattern of good models also shows positive (negative) potential over the central tropical Pacific as well as over the Southwest United States and negative (positive) potential over West Africa as well as over the extended Indian monsoon region at lower (upper) level, which is fairly consistent with the observed regression pattern as shown in Fig. 10a (Fig. 11a). On the contrary, poor models fail to show the divergence (convergence) over the Indian subcontinent at 850 hPa (150 hPa). They are showing feeble convergence over the tropical Pacific at 850 hPa, but fail to show divergence over south of the Equator at 150 hPa.

Figure 12 shows the regression maps of the unfiltered JJAS SLP onto the normalized low-pass filtered IPO index for observation as well as for good and poor CMIP5 models. In general, the Walker circulation is associated with low SLP over the western end of Pacific and high over the

eastern end. This basin-wide pressure gradient is the main driving force for the low-level zonal winds (i.e., the easterly trade winds) of the Walker circulation.

During the warm phase of IPO, the center of rising motion shifts east into the central-eastern Pacific, i.e., away from the western end of Pacific. This is consistent with the eastern Pacific warming signal as discussed earlier. This region is accompanied by low SLP, while the western end of Pacific will have high SLP, which is clearly seen in the observed IPO SLP regression pattern (Fig. 12a). This basin-wide pressure gradient (i.e., low pressure over the central-eastern tropical Pacific and high pressure over the western end of the Pacific) is the key driving force for the low-level westerly anomalies over the equatorial Pacific as seen in Fig. 9a.

The IPO SLP regression pattern shows positive anomalies over South Asia as well over Sahel, which is consistent with below-normal precipitation as discussed earlier. The composites of IPO SLP regression patterns for both good (Fig. 12b) and poor (Fig. 12c) CMIP5 models show positive SLP anomalies over India as well as over tropical Indian Ocean, though weaker in magnitude as compared to the observed regression pattern (Fig. 12a). The good models also reproduce the IPO SLP regression pattern over the tropical Pacific and Sahel, whereas the poor models fail to reproduce them.
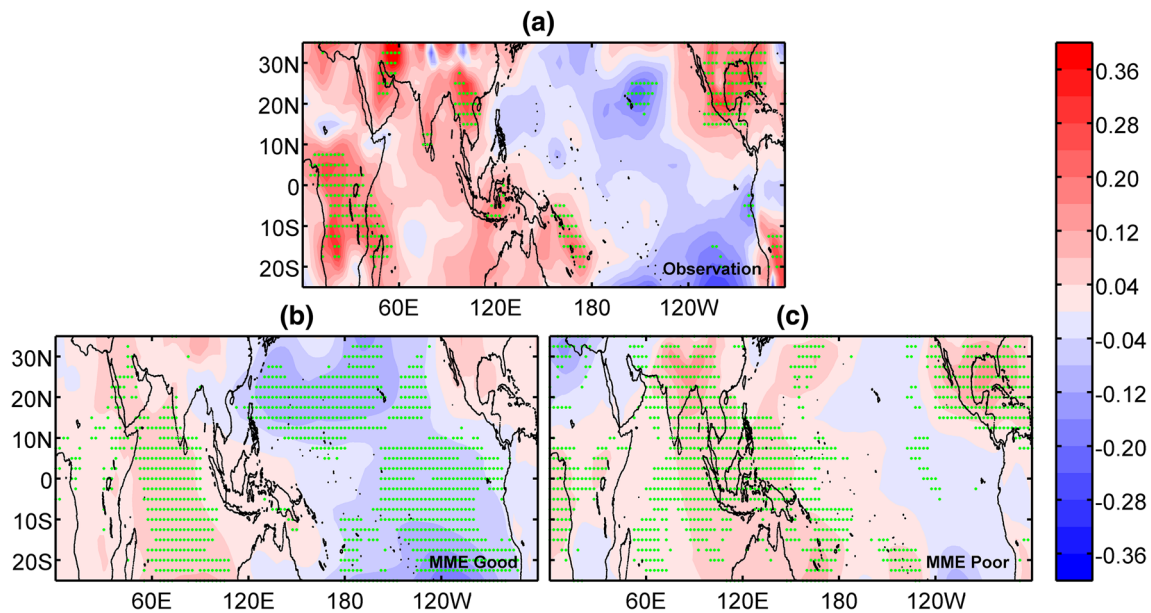
Fig. 12 a Regression of JJAS seasonal anomaly of SLP from NCEP/NCAR reanalysis (1948–1993) onto the standardized low-pass filtered IPO index. **b**, **c** Same as in Fig. 12a, but for the averaged regressions of 20 good and 12 poor CMIP5 models, respectively. The green stippling in observation indicates the grid point where the regression coefficient is statistically significant at 90 % confidence level, which is assessed via a two-tailed *t* test; whereas in MME good and MME poor it depicts the grid point where the sign of regression coefficient coincides in at least 15 out of the 20 good and 9 out of the 12 poor models, respectively. The unit of SLP is hPa per standard deviation

Overall atmospheric pattern associated with the IPO for good and poor models indicate that good models (and also observations) have a more pronounced alteration of the Walker circulation compared to poor models. This is also consistent with the fact that models with a larger zonal equatorial Pacific-Indian Ocean SST gradient also show larger negative precipitation responses over India, as discussed in Sect. 4.3. The tropical–extratropical Pacific SST gradient, which shows the strongest relation with Indian precipitation (see Fig. 8a), may contribute to enhance the Walker circulation response in the Indian Ocean in the good compared to the poor models (Fig. 11). The IPO SLP regression (Fig. 12) indicates low pressure in the subtropical western Pacific (around 20°N) for observations and the good models, whereas there is high pressure in the poor models. This feature may be responsible for a westward shifted and strengthened Walker circulation response in the good models compared to the poor models (e.g., Figure 11). It could be that the increased baroclinicity induced by the stronger SST gradient in the western Pacific plays a role in this response. However, the details of the mechanism for the tropical–extratropical SST gradient influence on the South Asian monsoon are still unclear and may be further investigated using idealized Atmospheric General Circulation Model (AGCM) simulations in a future study.

5 Summary and conclusion

In this study we have investigated the reproduction of the observed IPO-ISMR teleconnection in 32 CMIP5 models. Most models reproduce the IPO structure satisfactorily (with pattern correlation larger than 0.4), but with varying strength. Out of the 32 models considered about two-thirds also reproduce the observed negative IPO-ISMR relationship. In general, the models that fail to represent the IPO-ISMR teleconnection are the ones that are generally showing a poor spatial pattern of IPO, regardless of the extent to which they simulate the observed precipitation climatology and seasonal cycle. Considering models with good and poor reproduction of the IPO-ISMR teleconnection, we have identified the tropical–extratropical SST gradient in the IPO pattern as crucial parameter. Indeed, a scatter plot of the average rainfall regression over Indian land points versus the tropical–extratropical SST gradient in the IPO pattern shows a strong negative relationship between the two (CC −0.66), indicating that models with a strong tropical–extratropical IPO SST gradient also show a strong negative ISMR response over India. Also, the regression line is consistent with the observed IPO-ISMR relationship. On the other hand, several other scatter plots have also been considered, for example, the IPO precipitation regressions averaged over Indian land points versus

the IPO SST regressions averaged over (a) Niño 3.4, (b) Niño 4, and (c) Indian Ocean as well as (d) the difference between mean IPO SST regressions over Niño 3.4 region and Indian Ocean. For the first three scatter plots, the relationship is rather weak and not statistically significant. For the latter one the correlation becomes stronger (-0.45) and is statistically significant, but smaller than for the tropical–extratropical Pacific SST gradient. This signifies that the tropical–extratropical Pacific SST gradient is the most important feature for the good models, with some contribution also from the zonal equatorial Pacific-Indian Ocean SST gradient.

The composite of IPO wind regressions at 850 hPa (150 hPa) for good CMIP5 models reveals that the warm SSTAs in the equatorial tropical Pacific are associated with westerly (easterly) anomalies across the tropical Pacific, which is quite consistent with the observed regression pattern. The composite of IPO velocity potential regressions for good CMIP5 models at low (high) level depicts anomalous convergence (divergence) over the eastern-central tropical Pacific and Southwest United States and divergence (convergence) over the western end of Pacific extending to Indian subcontinent and West Africa. This is in agreement with the observed velocity potential regression pattern. On the contrary, the poor models fail to show the divergence (convergence) over the Indian subcontinent at 850 hPa (150 hPa). Furthermore, the averaged IPO SLP regression pattern for good CMIP5 models shows anomalous low over the eastern-central tropical Pacific and anomalous high over the western end of Pacific extending to Indian subcontinent and over South Africa, which is affiliated with low level convergence and divergence over the respective regions. In general, the CMIP5 models that are capable of reproducing the IPO-ISMR teleconnection also reasonably simulate the atmospheric circulation as well as the convergence/divergence patterns associated with the IPO.

The natural variability on decadal-to-multidecadal timescales in the Pacific Ocean, often referred to as IPO, affects the climatic conditions of India. This raises the possibility that the decadal SST variability of the Pacific, which is relatively smaller in variance as compared to ENSO, may provide supplementary information that will improve monsoon predictions over India. The decadal prediction generally focuses on time-evolving regional climatic conditions over the next 10–30 years, which is basically a time period of interest to infrastructure planners, water resource managers, and others. The predictions on decadal scale will in turn help society in improving the plans to mitigate the adverse effect of monsoon droughts or floods. The decadal time scale offers a critical bridge for informing adaptation strategies as climate varies and changes. Thus, for the better understanding of decadal-to-multidecadal variability as well as for improving the decadal predictions of rainfall

over India it is essential that the models should simulate the IPO skillfully.

Appendix

See Figs. 13 and 14.

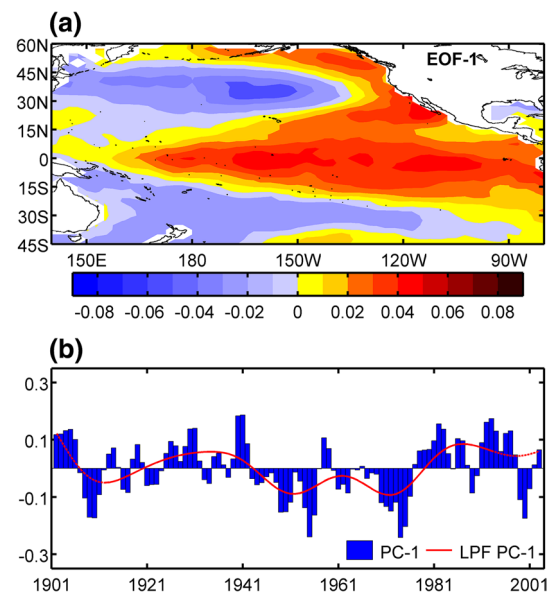**Fig. 13 a** The first EOF (EOF-1) of the detrended smoothed (3-year moving average) annual mean SSTAs computed over the Pacific basin (45°S–60°N, 140°E–80°W) and **b** the time series of the associated first principle component [PC-1; *blue bars* for annual data and the *red curve* is a smoothed time series obtained by applying Butterworth low-pass filter (order 4, cut-off frequency 21-year) to the annual bars]. The first and last 10-points of the filtered time series are ignored due to end effects of low-pass filter (shown by *dashed line*)
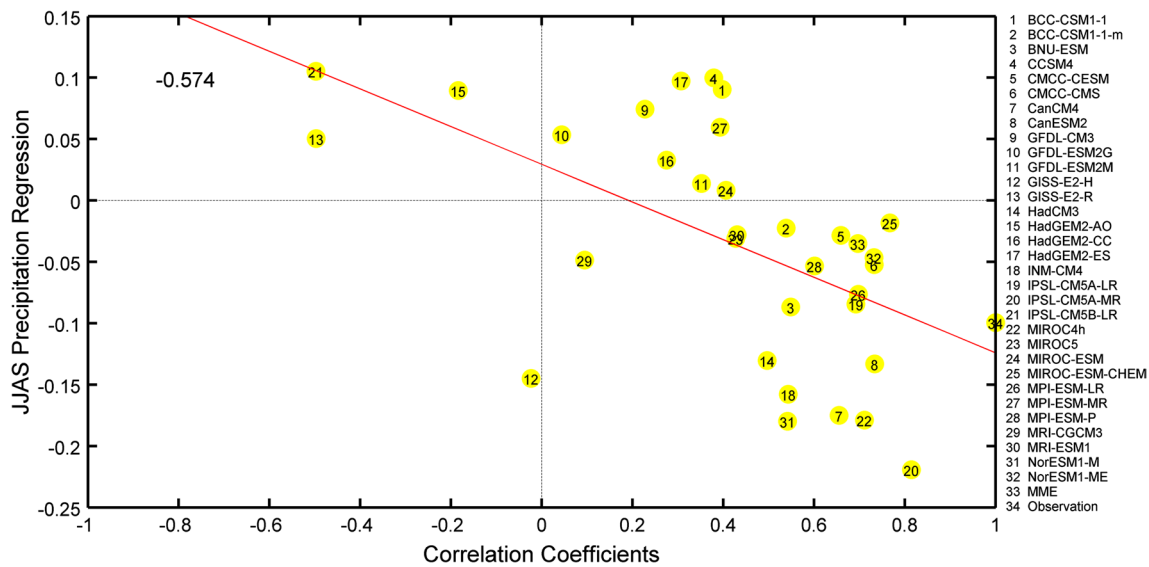
Fig. 14 Scatter plot between the IPO precipitation regressions (units are mm/d per standard deviation) averaged over Indian land points, excluding northeast region and correlation coefficients (shown in Fig. 4) representing the fidelity of CMIP5 models to simulate the IPO patterns

References

Alexander MA, Bladé I, Newman M, Lanzante JR, Lau N-C, Scott JD (2002) The atmospheric bridge: the influence of ENSO teleconnections on air–sea interaction over the global oceans. J Clim 15(16):2205–2231. doi:10.1175/1520-0442(2002)015<2205:tabtio>2.0.co;2

Allan RJ (2000) ENSO and climatic variability in the last 150 years. In: Diaz HF, Markgraf V (eds) El Niño and the Southern Oscillation: multiscale variability, global and regional impacts. Cambridge University Press, Cambridge, pp 3–56

Dai A (2013) The influence of the inter-decadal Pacific oscillation on US precipitation during 1923–2010. Clim Dyn 41(3–4):633–646. doi:10.1007/s00382-012-1446-5

Dong B, Dai A (2015) The influence of the Interdecadal Pacific Oscillation on temperature and precipitation over the Globe. Clim Dyn. doi:10.1007/s00382-015-2500-x

Dong L, Zhou T, Chen X (2014) Changes of Pacific decadal variability in the twentieth century driven by internal variability, greenhouse gases, and aerosols. Geophys Res Lett 41(23):8570–8577. doi:10.1002/2014gl062269

Feudale L, Kucharski F (2013) A common mode of variability of African and Indian monsoon rainfall at decadal timescale. Clim Dyn 41(2):243–254. doi:10.1007/s00382-013-1827-4

Folland CK, Salinger MJ (1995) Surface temperature trends and variations in New Zealand and the surrounding ocean, 1871–1993. Int J Climatol 15(11):1195–1218. doi:10.1002/joc.3370151103

Folland CK, Parker DE, Colman AW, Washington R (1999) Large scale modes of ocean surface temperature since the late nineteenth century. In: Navarra A (ed) Beyond El Niño: decadal and interdecadal climate variability. Springer, Berlin, pp 73–102

Fuentes-Franco R, Giorgi F, Coppola E, Kucharski F (2015) The role of ENSO and PDO in variability of winter precipitation over North America from twenty first century CMIP5 projections. Clim Dyn. doi:10.1007/s00382-015-2767-y

Gershunov A, Barnett TP (1998) Interdecadal modulation of ENSO teleconnections. Bull Am Meteorol Soc 79(12):2715–2725. doi:10.1175/1520-0477(1998)079<2715:imoet>2.0.co;2

Goswami BN (2005) Interdecadal variability. In: Wang B (ed) The Asian monsoon. Praxis, Springer, Berlin, pp 295–327

Harris I, Jones PD, Osborn TJ, Lister DH (2014) Updated high-resolution grids of monthly climatic observations—the CRU TS3.10 dataset. Int J Climatol 34(3):623–642. doi:10.1002/joc.3711

Huffman GJ, Adler RF, Bolvin DT, Gu G (2009) Improving the global precipitation record: GPCP Version 2.1. Geophys Res Lett. doi:10.1029/2009gl040000

Joshi MK, Pandey AC (2011) Trend and spectral analysis of rainfall over India during 1901–2000. J Geophys Res Atmos 116(D6):D06104. doi:10.1029/2010jd014966

Joshi MK, Rai A (2015) Combined interplay of the Atlantic multidecadal oscillation and the Interdecadal Pacific Oscillation on rainfall and its extremes over Indian subcontinent. Clim Dyn 44(11–12):3339–3359. doi:10.1007/s00382-014-2333-z

Kalnay E, Kanamitsu M, Kistler R, Collins W, Deaven D, Gandin L, Iredell M, Saha S, White G, Woollen J, Zhu Y, Leetmaa A, Reynolds R, Chelliah M, Ebisuzaki W, Higgins W, Janowiak J, Mo KC, Ropelewski C, Wang J, Jenne R, Joseph D (1996) The NCEP/NCAR 40-year reanalysis project. Bull Am Meteorol Soc 77(3):437–471. doi:10.1175/1520-0477(1996)077<0437:tnyrp>2.0.co;2

Kripalani RH, Kulkarni A, Singh SV (1997) Association of the Indian summer monsoon with the northern hemisphere mid-latitude circulation. Int J Climatol 17(10):1055–1067. doi:10.1002/(sici)1097-0088(199708)17:10<1055:aid-joc180>3.0.co;2-3

Krishnamurthy V, Goswami BN (2000) Indian monsoon–ENSO relationship on interdecadal timescale. J Clim 13(3):579–595. doi:10.1175/1520-0442(2000)013<0579:imeroi>2.0.co;2

Krishnamurthy L, Krishnamurthy V (2014) Influence of PDO on South Asian summer monsoon and monsoon–ENSO relation. Clim Dyn 42(9–10):2397–2410. doi:10.1007/s00382-013-1856-z

Krishnan R, Sugi M (2003) Pacific decadal oscillation and variability of the Indian summer monsoon rainfall. Clim Dyn 21(3–4):233–242. doi:10.1007/s00382-003-0330-8

Kucharski F, Scaife AA, Yoo JH, Folland CK, Kinter J, Knight J, Fereday D, Fischer AM, Jin EK, Kröger J, Lau NC, Nakaegawa T, Nath MJ, Pegion P, Rozanov E, Schubert S, Sporyshev PV,

Syktus J, Voldoire A, Yoon JH, Zeng N, Zhou T (2009) The CLI-VAR C20C project: skill of simulating Indian monsoon rainfall on interannual to decadal timescales. Does GHG forcing play a role? Clim Dyn 33(5):615–627. doi:10.1007/s00382-008-0462-y

Mantua NJ, Hare SR, Zhang Y, Wallace JM, Francis RC (1997) A Pacific Interdecadal Climate Oscillation with impacts on salmon production. Bull Am Meteorol Soc 78(6):1069–1079. doi:10.1175/1520-0477(1997)078<1069:apicow>2.0.co;2

Meehl GA, Hu A (2006) Megadroughts in the Indian Monsoon Region and Southwest North America and a mechanism for associated multidecadal Pacific Sea surface temperature anomalies. J Clim 19(9):1605–1623. doi:10.1175/jcli3675.1

Meehl GA, Hu A, Santer BD (2009) The mid-1970s climate shift in the Pacific and the relative roles of forced versus inherent decadal variability. J Clim 22(3):780–792. doi:10.1175/2008jcli2552.1

Meehl GA, Hu A, Arblaster JM, Fasullo J, Trenberth KE (2013) Externally forced and internally generated decadal climate variability associated with the Interdecadal Pacific Oscillation. J Clim 26(18):7298–7310. doi:10.1175/jcli-d-12-00548.1

Mohino E, Janicot S, Bader J (2011) Sahel rainfall and decadal to multi-decadal sea surface temperature variability. Clim Dyn 37(3–4):419–440. doi:10.1007/s00382-010-0867-2

Polade SD, Gershunov A, Cayan DR, Dettinger MD, Pierce DW (2013) Natural climate variability and teleconnections to precipitation over the Pacific-North American region in CMIP3 and CMIP5 models. Geophys Res Lett 40(10):2296–2301. doi:10.1002/grl.50491

Power S, Tseitkin F, Torok S, Lavery B, Dahni R, McAvaney B (1998) Australian temperature, Australian rainfall and the Southern Oscillation, 1910–1992: coherent variability and recent changes. Aust Meteorol Mag 47(2):85–101

Power S, Casey T, Folland C, Colman A, Mehta V (1999) Inter-decadal modulation of the impact of ENSO on Australia. Clim Dyn 15(5):319–324. doi:10.1007/s003820050284

Rajeevan M, Bhate J, Jaswal AK (2008) Analysis of variability and trends of extreme rainfall events over India using 104 years of gridded daily rainfall data. Geophys Res Lett 35:L18707. doi:10.1029/2008GL035143

Rasmusson EM, Carpenter TH (1983) The relationship between eastern equatorial Pacific sea surface temperatures and rainfall over India and Sri Lanka. Mon Weather Rev 111(3):517–528. doi:10.1175/1520-0493(1983)111<0517:trbeep>2.0.co;2

Rayner NA, Parker DE, Horton EB, Folland CK, Alexander LV, Rowell DP, Kent EC, Kaplan A (2003) Global analyses of sea surface temperature, sea ice, and night marine air temperature since the late nineteenth century. J Geophys Res Atmos 108(D14):4407. doi:10.1029/2002jd002670

Salinger MJ, Mullan AB (1999) New Zealand climate: temperature and precipitation variations and their links with atmospheric circulation 1930–1994. Int J Climatol 19(10):1049–1071. doi:10.1002/(sici)1097-0088(199908)19:10<1049:aid-joc417>3.0.co;2-z

Sheffield J, Camargo SJ, Fu R, Hu Q, Jiang X, Johnson N, Karnauskas KB, Kim ST, Kinter J, Kumar S, Langenbrunner B, Maloney E, Mariotti A, Meyerson JE, Neelin JD, Nigam S, Pan Z, Ruiz-Barradas A, Seager R, Serra YL, Sun D-Z, Wang C, Xie S-P, Yu J-Y, Zhang T, Zhao M (2013) North American climate in CMIP5 experiments. Part II: evaluation of historical simulations of intraseasonal to decadal variability. J Clim 26(23):9247–9290. doi:10.1175/jcli-d-12-00593.1

Shukla J (1987) Interannual variability of monsoons. In: Fein JS, Stephens PL (eds) Monsoons. Wiley, New York, pp 399–463

Shukla J, Paolino DA (1983) The Southern Oscillation and long-range forecasting of the summer monsoon rainfall over India. Mon Weather Rev 111(9):1830–1837. doi:10.1175/1520-0493(1983)111<1830:tsoalr>2.0.co;2

Taylor KE (2001) Summarizing multiple aspects of model performance in a single diagram. J Geophys Res Atmos 106(D7):7183–7192. doi:10.1029/2000jd900719

Taylor KE, Stouffer RJ, Meehl GA (2012) An overview of CMIP5 and the experiment design. Bull Am Meteorol Soc 93(4):485–498. doi:10.1175/bams-d-11-00094.1

Trenberth K, Hurrell J (1994) Decadal atmosphere-ocean variations in the Pacific. Clim Dyn 9(6):303–319. doi:10.1007/bf00204745

Villamayor J, Mohino E (2015) Robust Sahel drought due to the Interdecadal Pacific Oscillation in CMIP5 simulations. Geophys Res Lett 42(4):1214–1222. doi:10.1002/2014gl062473

Wang B, Liu J, Kim H-J, Webster PJ, Yim S-Y, Xiang B (2013) Northern Hemisphere summer monsoon intensified by mega-El Niño/southern oscillation and Atlantic multidecadal oscillation. Proc Natl Acad Sci USA 110(14):5347–5352. doi:10.1073/pnas.1219405110

Zhang Y, Wallace JM, Battisti DS (1997) ENSO-like interdecadal variability: 1900–1993. J Clim 10(5):1004–1020. doi:10.1175/1520-0442(1997)010<1004:eliv>2.0.co;2